analytical chemistry

pubs.acs.org/ac Article

Photoelectrochemical Immunosensor Based on a 1D Fe_2O_3/3D Cd-$ZnIn_{2.2}S_y$ Heterostructure as a Sensing Platform for Ultrasensitive Detection of Neuron-Specific Enolase

Jingui Chen, Jinxiu Zhao, Jinhui Feng, Dan Wu, Hongmin Ma, Xiang Ren,* Qin Wei, and Huangxian Ju

Cite This: *Anal. Chem.* 2022, 94, 17396−17404 Read Online

ACCESS | Metrics & More | Article Recommendations | Supporting Information

ABSTRACT: Lung cancer is a high-mortality cancer related to the concentration of neuron-specific enolase (NSE). In this work, a sandwich-type photoelectrochemical (PEC) immunosensor was constructed for ultrasensitive detection of NSE, which is based on iron trioxide/indium zinc cadmium sulfide (Fe_2O_3/Cd-$ZnIn_{2.2}S_y$) as a sensing platform and Ag-modified polyaniline (Ag@PANI) as a signal amplification label. The 1D Fe_2O_3 porous nanorods with a large specific surface area were synthesized by calcination of Fe-MIL-88A and etching of NaOH. To improve the photocurrent response, the 3D architecture Cd-$ZnIn_{2.2}S_y$ was combined with the 1D Fe_2O_3 porous nanorods to form a 1D Fe_2O_3/3D Cd-$ZnIn_{2.2}S_y$ heterostructure. Specifically, the Fe_2O_3/Cd-$ZnIn_{2.2}S_y$ heterostructure with a good energy level matching (the two can form a stepped energy level matching, which accelerates the transfer rate of electrons) can improve the separation efficiency of electron−hole pairs (e^-/h^+) under visible light irradiation, which enhances the photocurrent response. Ag@PANI has a strong electron transport capability and can be used as a secondary antibody marker for the signal amplification of the immunosensor. The sensor exhibits a good linear detection range of 100 fg/mL to 100 ng/mL with a low detection limit of 33.5 fg/mL. Moreover, the constructed sandwich-type PEC immunosensor shows good performance and possesses excellent specificity, selectivity, and stability over a period of 4 weeks for NSE detection. With these excellent properties, the immunosensor can be extended to analyze and diagnose other disease biomarkers.

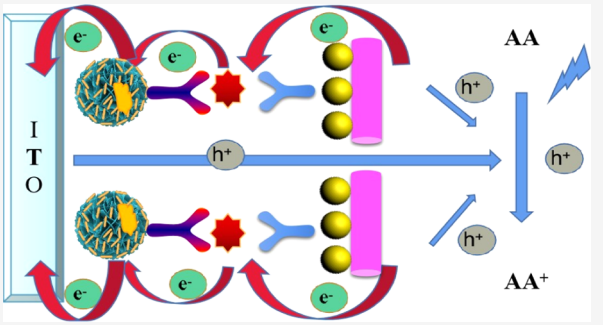

INTRODUCTION

Lung cancer is one of the most common cancers that is divided into small-cell lung cancer and non-small-cell lung cancer, of which the prevalence of small-cell lung cancer is relatively high.[1] The symptoms of lung cancer do not appear in the early stage, and most patients are already in the middle and late stages when the symptoms are obvious. It is meaningful to screen for lung cancer whose mortality rate in the middle and late stages is very high.[2] Among them, the occurrence of small-cell lung cancer is related to the concentration of neuron-specific enolase (NSE), which leads to an abnormally high concentration (100 ng/mL) of serum NSE.[3−5] Therefore, there is a need to establish a method that can detect NSE in human serum rapidly and sensitively.

There are many methods for NSE detection, including chemiluminescent aptamers,[6] the ionic liquid method,[4] surface plasmon resonance,[7] and Raman scattering assays.[5] Although these methods have a wide detection range, sometimes the operation is complex. With the development of modern bioanalytical methods, photoelectrochemical (PEC) analysis stands out as an emerging detection technology.[8,9] In addition, PEC immunosensors offer a low background signal due to the effective separation of the excitation source and the detection signal.[10] At the same time, PEC immunosensors have been used for the detection of various biological substances with the advantages of simple instrumentation, short reaction time, and high sensitivity.[11] The excellent photoelectric conversion efficiency of a PEC immunosensor is determined by the excellent chemical properties of the substrate material. Additionally, the photoactive semiconductor materials are an important component of PEC immunosensors that affect the photoelectric conversion efficiency.

Recently, a wide variety of photoactive semiconductor materials have been used in the fields of photocatalysis, photodegradation, and sensor analysis.[12] In particular, Fe_2O_3, as an oxide semiconductor material, has a wide range of applications to PEC analysis because of its good photocatalytic properties in visible light.[13] In addition, it offers excellent advantages of diverse morphology, high natural abundance,

Received: June 20, 2022
Accepted: November 22, 2022
Published: December 6, 2022

https://doi.org/10.1021/acs.analchem.2c02645
Anal. Chem. 2022, 94, 17396−17404

and a suitable bandgap of 2.2 eV.[14,15] However, the photocurrent response of most semiconductors is weaker than that of compound semiconductor materials. Many strategies have been developed to improve the photocurrent response of PEC immunosensors, such as surface modification, surface passivation,[16] morphology control,[17] formation of heterojunction structures,[16,18] and metal doping.[19] Among them, heterojunction and metal doping are the foci of semiconductor modification. A heterojunction can promote the rapid transfer of photogenerated carriers because of its special interface structure (close to an ideal diode) and thus improve the photocurrent response.[20] A metal-doped semiconductor can inhibit the recombination of an electron (e^-) and a hole (h^+) and effectively promote the charge separation, enhancing the e^-/h^+ pair separation efficiency. $ZnIn_{2.2}S_y$ (as the states of S are S_2^{2-} and S^{2-}, y is used to denote the stoichiometric uncertainty) is a sulfide semiconductor material with a large surface area and high stability, and the highest photoelectric conversion efficiency of 3.10% is achieved at a ratio of 1:2.2 of Zn/In.[21] In addition, the metal Cd^{2+} doping of $ZnIn_{2.2}S_y$ forms a Cd-$ZnIn_{2.2}S_y$ structure that suppresses the charge recombination and further improves the e^-−h^+ pair separation efficiency.[19,22] Furthermore, Cd-$ZnIn_{2.2}S_y$ with a 3D flower-like nanostructure has abundant surface area to provide many reaction sites and also improves the photon utilization by reducing the photon losses due to reflection and scattering.[23] Thus, Fe_2O_3 and Cd-$ZnIn_{2.2}S_y$ can be combined to form a 1D Fe_2O_3/3D Cd-$ZnIn_{2.2}S_y$ heterojunction composite to improve the weak photocurrent response of individual semiconductors.

In this work, a sandwich-type PEC immunosensor was designed to achieve sensitive detection of NSE. The 1D Fe_2O_3/3D Cd-$ZnIn_{2.2}S_y$ heterojunction composite was used as the substrate material for improving the photocurrent response. Even though the substrate material has a strong photocurrent response, good linearity is not obtained at very low concentrations of some analytes to be detected. Therefore, signal amplification strategies play an important role in the development of a highly sensitive PEC immunoassay system. In this respect, polyaniline (PANI) was used in this work as a conductive polymer with properties including strong catalytic activity in light, strong ability to transfer carriers, low cost, and good chemical stability.[24] To improve the electrical conductivity, PANI was modified with a Ag@PANI label (Ag@PANI-Ab_2), which has an excellent electrical conductivity and good photocatalytic properties. The concentration of Ag@PANI-Ab_2 will increase with the antigen concentration, which then increases the PEC photocurrent (51.5% enhanced). In this way, a PEC immunosensor with a Ag@PANI label for signal amplification was constructed successfully. A calibration plot relating current signal obtained as a function of antigen concentration can then be constructed for sensitive detection and quantitative analysis of NSE. The excellent performance of this PEC immunosensor offers promise for the detection of other biomarkers.

EXPERIMENTAL SECTION

Reagents and Apparatus. The reagents and apparatus used in this study are reported in the Supporting Information.

Preparation of Fe_2O_3 Nanorods. Fe_2O_3 nanorods were synthesized by calcining the precursor of Fe-MIL-88A ($C_{12}H_6O_{13}Fe_3$).[15] Specifically, 1.28 g of $Fe(NO_3)_3{\cdot}9H_2O$ and 0.336 g of fumaric acid were dissolved in 60 mL of dimethyl formamide and heated in an oil bath at 110 °C for 30 min. The sample of Fe-MIL-88A was obtained after washing with dimethylformamide and methanol three times and drying under vacuum at 60 °C for 8 h. Afterward, 0.05 g of Fe-MIL-88A was dispersed in a solution containing 25 mL of ultrapure water and 75 mL of ethanol, which was then sonicated for 10 min. Then, 20 mL of the 0.8 mol/L sodium hydroxide solution was added dropwise and stirred for 4.5 h. The reddish-brown product was washed with ethanol and ultrapure water three times. Finally, the etched Fe-MIL-88A was placed in a muffle furnace and calcined at 500 °C for 4 h to obtain Fe_2O_3 nanorods.

Synthesis of Fe_2O_3/Cd-$ZnIn_{2.2}S_y$. Fe_2O_3/Cd-$ZnIn_{2.2}S_y$ was prepared by a hydrothermal synthesis method. Specifically, 0.04 g of Fe_2O_3 was dissolved by ultrasonicating in 30 mL of ultrapure water for 10 min. Then, 0.0366 g of $ZnCl_2$, 0.0604 g of thiourea, and 0.1317 g of $InCl_3$ were added into the Fe_2O_3 solution and stirred for 5 h. The above mixed suspension solution was placed in an autoclave and maintained at 160 °C for 6 h. After that, it was washed three times with ultrapure water and ethanol, dried under vacuum, ground, and stored in a centrifuge tube. Finally, 0.018 g of Fe_2O_3/$ZnIn_{2.2}S_y$ was added to an aqueous $CdCl_2$ (10 mL, 0.1 mol/L) solution, stirred for 5 h, and washed with ultrapure water and ethanol to obtain the Fe_2O_3/Cd-$ZnIn_{2.2}S_y$ nanocomposite.

Preparation of Ag@PANI-Ab_2. PANI was obtained by solution polymerization. First, 1.86 g of aniline and 18 mL of hydrochloric acid were added to 100 mL of deionized water. In addition, 4.56 g of $(NH_4)_2S_2O_8$ (0.2 M) was dissolved in 100 mL of the above-mentioned aqueous solution and added dropwise to the aniline solution to polymerize for 3 h to obtain PANI. Then, the precipitate was washed by centrifugation and dried in a vacuum-drying oven at 60 °C for 8 h. Then, 0.1 g of PANI was added to 50 mL of ultrapure water, sonicated for 20 min, and stirred for 30 min. Ag@PANI was obtained by an in situ reduction reaction. First, 0.016 g of $AgNO_3$ was dissolved in the PANI solution and shaken for 2 h. Then, 4 mL of 0.05 mol/L trisodium citrate ($C_6H_5Na_3O_7$) was added dropwise to the above solution and shaken for 3 h. After washing the precipitate with ultrapure water and ethanol, the Ag@PANI composite nanomaterial was obtained. Then, Ag@PANI (3 mL, 1 mg/mL) and Ab_2 solution (1 mL, 10 μg/mL) were incubated at 4 °C for 12 h. Finally, the incubated Ag@PANI-Ab_2 was washed and redispersed in a 0.1 M phosphate-buffered saline (PBS; pH 7.4) for future use.

Construction of a Sandwich-Type PEC Immunosensor. Scheme 1 shows the construction process of a PEC immunosensor. First, an indium tin oxide (ITO) glass was successively washed with acetone, ethanol, sodium hydroxide, and ultrapure water for 25 min and dried with nitrogen before use. Then, 30 μL of the Fe_2O_3/Cd-$ZnIn_{2.2}S_y$ suspension was applied to the ITO glass surface. Subsequently, it was placed in a muffle furnace and calcined at 200 °C for 5 h to obtain an ITO/Fe_2O_3/Cd-$ZnIn_{2.2}S_y$ electrode. Then, the ITO/Fe_2O_3/Cd-$ZnIn_{2.2}S_y$ electrode was incubated in 4 mg/mL polydopamine (PDA) Tris-HCI solution (pH 8.5) for 10 h, washed with ultrapure water, and dried. After that, 10 μL of the primary antibody Ab_1 was applied to the surface of the ITO/Fe_2O_3/Cd-$ZnIn_{2.2}S_y$ electrode and incubated at 4 °C for 2 h; then, the excess Ab_1 was washed off with 0.1 mol/L PBS (pH 7.4). Afterward, we added 6 μL of bovine albumin serum (BSA, 1 wt %) onto the above-modified electrode and incubated it for 2 h to shield non-specific active sites. Subsequently, 10 μL of different concentrations of NSE was

https://doi.org/10.1021/acs.analchem.2c02645
Anal. Chem. 2022, 94, 17396−17404

Scheme 1. Schematic Diagram of the Construction of the Sandwich-Type PEC Immunosensor

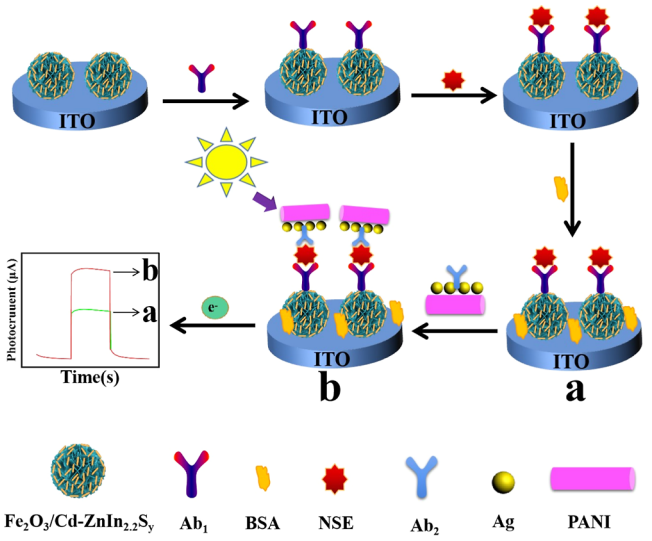

added and incubated for 2 h at 4 °C in a refrigerator. Finally, 10 μL of the Ag@PANI-conjugated secondary antibody (Ag@PANI-Ab_2) was added to the above PEC sensing electrode to construct a sandwich-type PEC immunosensor. All the cleaning procedures were rinsed with PBS to remove nonspecific adsorption.

PEC Measurement and Detection Mechanism. The measurement system was a three-electrode system with the prepared ITO electrode acting as the working electrode, a platinum electrode as the counter electrode, and a saturated calomel electrode as the reference electrode (warning: the saturated calomel reference electrode must be handled with care owing to the health risks arising from mercury vapor in the electrode).

The PEC reaction was measured in 10 mL of PBS containing appropriate concentrations of ascorbic acid (AA). A current (I) versus time (t) signal was used as the output signal for photoelectric detection, an LED lamp was used as the light source, and the bias voltage was set to zero.

RESULTS AND DISCUSSION

Characterization of Fe_2O_3, Fe_2O_3/Cd-$ZnIn_{2.2}S_y$, and Ag@PANI. The substrate material is critical for the basis of PEC. Therefore, the substrate material was first analyzed and characterized. The morphologies of Fe_2O_3 and Fe_2O_3/Cd-$ZnIn_{2.2}S_y$ were characterized by scanning electron microscopy (SEM). As shown in Figure 1A, Fe_2O_3 was obtained by calcination of Fe-MIL-88. As shown in Figure S1A, Fe-MIL-88A is a regularly shaped rodlike structure of size 300−350 nm. In Figure 1B, it is shown that the Cd-$ZnIn_{2.2}S_y$ nanomaterial wraps around the Fe_2O_3 nanorods to form a heterojunction surface, indicating that the synthesis of the Fe_2O_3/Cd-$ZnIn_{2.2}S_y$ nanocomposite is successful. As shown in Figure S2, the energy-dispersive spectroscopy (EDS) spectra of the six elements Fe, O, S, Zn, In, and Cd are uniformly distributed in the elemental distribution map. As shown in Figure S3, the EDS pattern of the six elements Fe, O, S, Zn, In, and Cd shows their uniform distribution in the Fe_2O_3/Cd-$ZnIn_{2.2}S_y$ sample. In addition, the atomic ratio of Cd/Zn/In is 0.4:1:3 in Table S1, which is due to the partial substitution of Zn^{2+} by Cd^{2+}. On the basis of the atomic percentage values given in Table S1, the sum of the atomic percentage of the Cd element and the Zn element is 3.94%, the atomic percentage of the In element is 8.62%, and the ratio of the two is 1:2.2. It is calculated that the atomic ratio of Zn/In before doping with Cd is 1:2.2, further indicating the synthesis of Fe_2O_3/Cd-$ZnIn_{2.2}S_y$. The crystallinity of Fe_2O_3 and the Fe_2O_3/Cd-

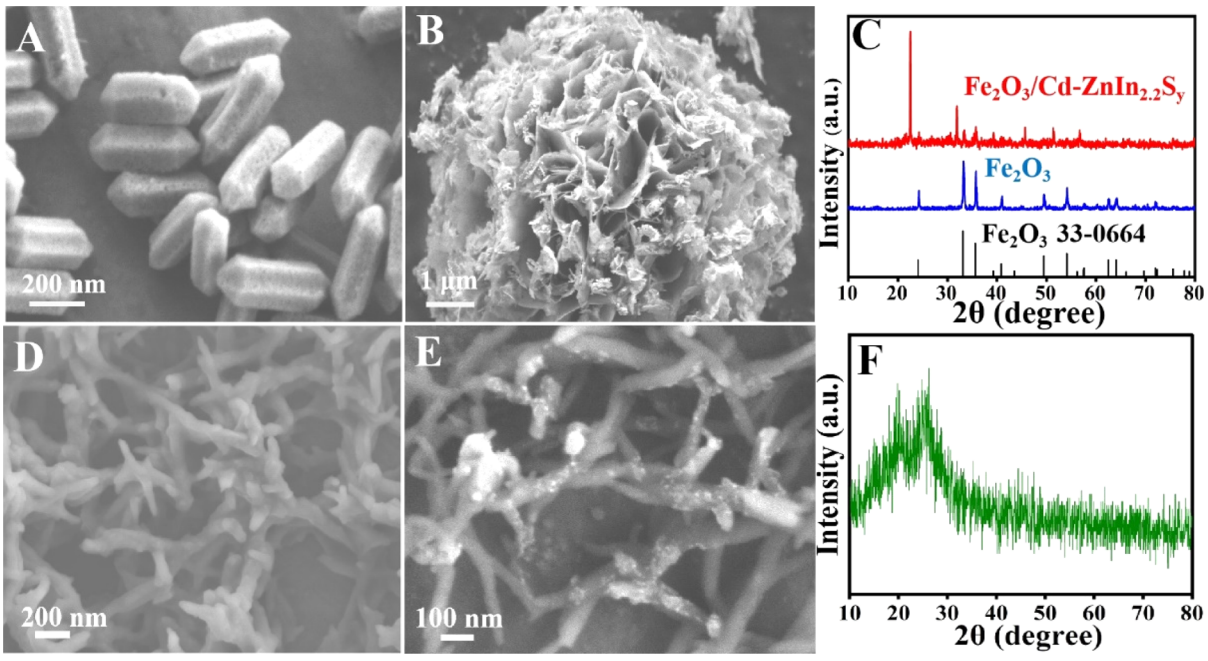

Figure 1. (A) Scanning electron micrograph of Fe_2O_3, (B) scanning electron micrograph of Fe_2O_3/Cd-$ZnIn_{2.2}S_y$, (C) X-ray diffraction (XRD) patterns of Fe_2O_3 and Fe_2O_3/Cd-$ZnIn_{2.2}S_y$, (D) scanning electron micrograph of PANI, (E) scanning electron micrograph of Ag@PANI, and (F) XRD pattern of PANI.

https://doi.org/10.1021/acs.analchem.2c02645
Anal. Chem. 2022, 94, 17396−17404

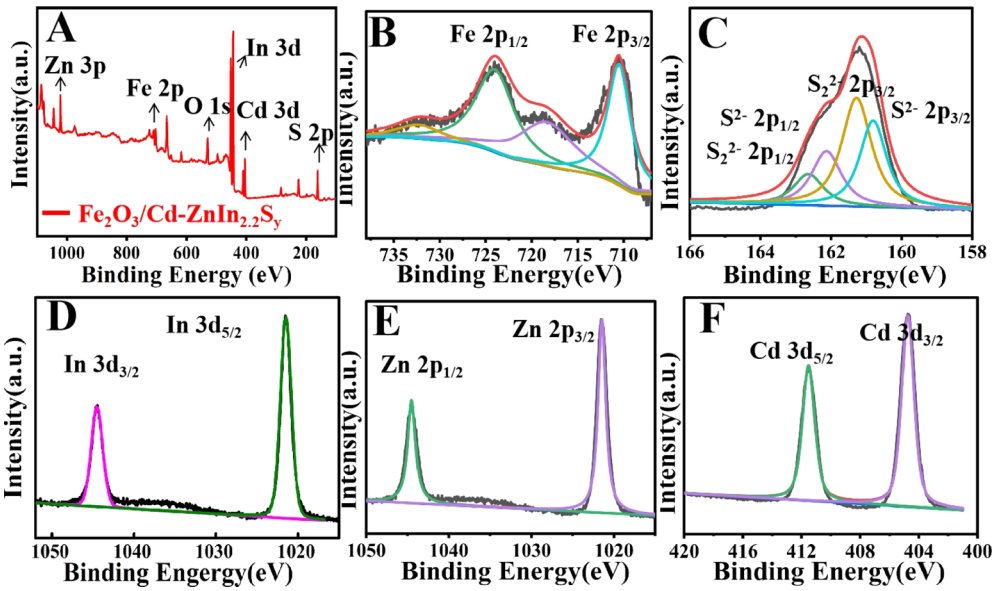

Figure 2. (A) X-ray photoelectron survey spectrum of the Fe_2O_3/Cd-$ZnIn_{2.2}S_y$ composite; high-resolution X-ray photoelectron spectrum for (B) Fe 2p, (C) S 2p, (D) In 3d, (E) Zn 2p, and (F) Cd 3d.

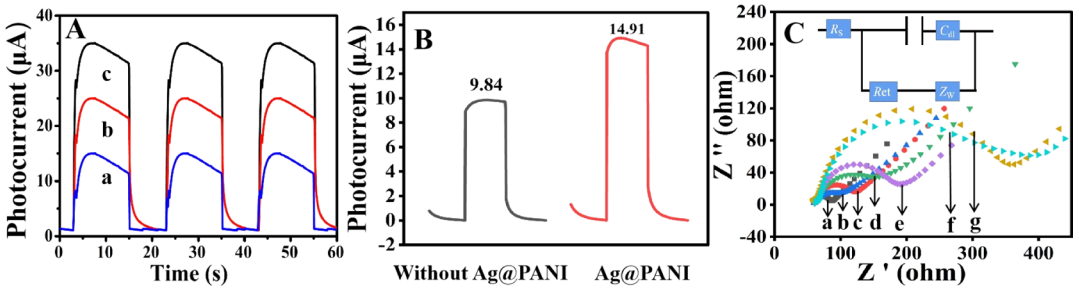

Figure 3. (A) Photocurrent vs time plot of 0.1 M ascorbic acid at Fe_2O_3 [trace (a)], Fe_2O_3−$ZnIn_{2.2}S_y$ [trace (b)], and Fe_2O_3/Cd-$ZnIn_{2.2}S_y$ [trace (c)]; (B) photocurrent comparison before and after marking Ag@PANI; and (C) electrochemical impedance spectra of 5 mM $[Fe(CN)_6]^{4-/3-}$ and 10 ng/mL NSE at the bare ITO [trace (a)], ITO/Fe_2O_3/Cd-$ZnIn_{2.2}S_y$ [trace (b)], ITO/Fe_2O_3/Cd-$ZnIn_{2.2}S_y$/PDA [trace (c)], ITO/Fe_2O_3/Cd-$ZnIn_{2.2}S_y$/PDA/Ab_1 [trace (d)], ITO/Fe_2O_3/Cd-$ZnIn_{2.2}S_y$/PDA/Ab_1/BSA [trace (e)], ITO/Fe_2O_3/Cd-$ZnIn_{2.2}S_y$/PDA/Ab_1/BSA/NSE [trace (f)], and ITO/Fe_2O_3/Cd-$ZnIn_{2.2}S_y$/PDA/Ab_1/BSA/NSE/Ag@PANI-Ab_2 [trace (g)].

$ZnIn_{2.2}S_y$ nanocomposite was analyzed by XRD, and the results are shown in Figure 1C. The diffraction peaks in the spectra of Fe_2O_3 and Fe_2O_3/Cd-$ZnIn_{2.2}S_y$ matched well with the hexagonal Fe_2O_3 standard card (JCPDS 33-0664). In contrast, a new diffraction peak appears at 22° for the Fe_2O_3/Cd-$ZnIn_{2.2}S_y$ composite, which corresponds to the diffraction pattern of $ZnIn_{2.2}S_y$. The main diffraction peak of Fe_2O_3 in Fe_2O_3/Cd-$ZnIn_{2.2}S_y$ is slightly reduced, which might be due to the presence of Cd-$ZnIn_{2.2}S_y$. The characterization results indicate that Fe_2O_3 and the Fe_2O_3/Cd-$ZnIn_{2.2}S_y$ nanocomposite are successfully synthesized. The morphology of PANI and Ag@PANI was characterized by SEM. As shown in Figure 1D, the PANI nanomaterial has a nanorod-like structure, and the Ag nanoparticles are uniformly loaded on the surface of PANI, indicating that the Ag nanoparticles were loaded on PANI by in situ reduction, as shown in Figure 1E. Meanwhile, the crystallinity of the prepared PANI nanomaterial was analyzed by XRD, and the results obtained are shown in Figure 1F, where a broad diffraction peak was observed between 10 and 30°, which confirmed that PANI grew in an amorphous state. Figure 2A shows the X-ray photoelectron spectrum obtained in investigating the surface atomic compositions and chemical states of the elements in the Fe_2O_3/Cd-$ZnIn_{2.2}S_y$ composite. The elements Fe, O, S, In, Zn, and Cd appear in the full XPS survey spectrum. The X-ray photoelectron spectrum for O in Figure S4 shows two O peaks at 529.5 and 531.5 eV, which are assigned to Fe−O and −OH, respectively. As shown in Figure 2B, the two diffraction peaks of Fe at 724.1 and 710.5 eV are designated as Fe $2p_{1/2}$ and Fe $2p_{3/2}$, respectively. Besides, there are two satellite peaks (732.3 and 718.2 eV) at higher binding energies, demonstrating the presence of Fe^{3+}.[15] In Figure 2C, it is shown that the two peaks at 160.8 and 162.2 eV, respectively, correspond to $2p_{3/2}$ and $2p_{1/2}$ of S^{2-}. The peaks at 161.3 and 162.8 eV correspond to $2p_{3/2}$ and $2p_{1/2}$ of S_2^{2-}. In Figure 2D, it is shown that the two peaks at 452.8 and 444.8 eV correspond to $3d_{3/2}$ and $3d_{5/2}$ of In, respectively, suggesting the presence of In. In Figure 2E, it is shown that the peaks at 1045.2 and 1022.1 eV correspond to $2p_{1/2}$ and $2p_{3/2}$ of Zn, respectively.[25] In Figure 2F, it is shown that the 411.5 and 404.7 eV peaks correspond to $3d_{5/2}$ and $3d_{3/2}$ of Cd, respectively. These results are indicative of the success of the Fe_2O_3/Cd-$ZnIn_{2.2}S_y$ composite preparation.[26]

Comparison of the PEC Signal. To verify whether the PEC signal is increased, we compared the current signal obtained at Fe_2O_3-, Fe_2O_3/$ZnIn_{2.2}S_y$-, and Fe_2O_3/Cd-$ZnIn_{2.2}S_y$-coated ITO. The electrolyte was 10 mL of PBS

https://doi.org/10.1021/acs.analchem.2c02645
Anal. Chem. 2022, 94, 17396−17404

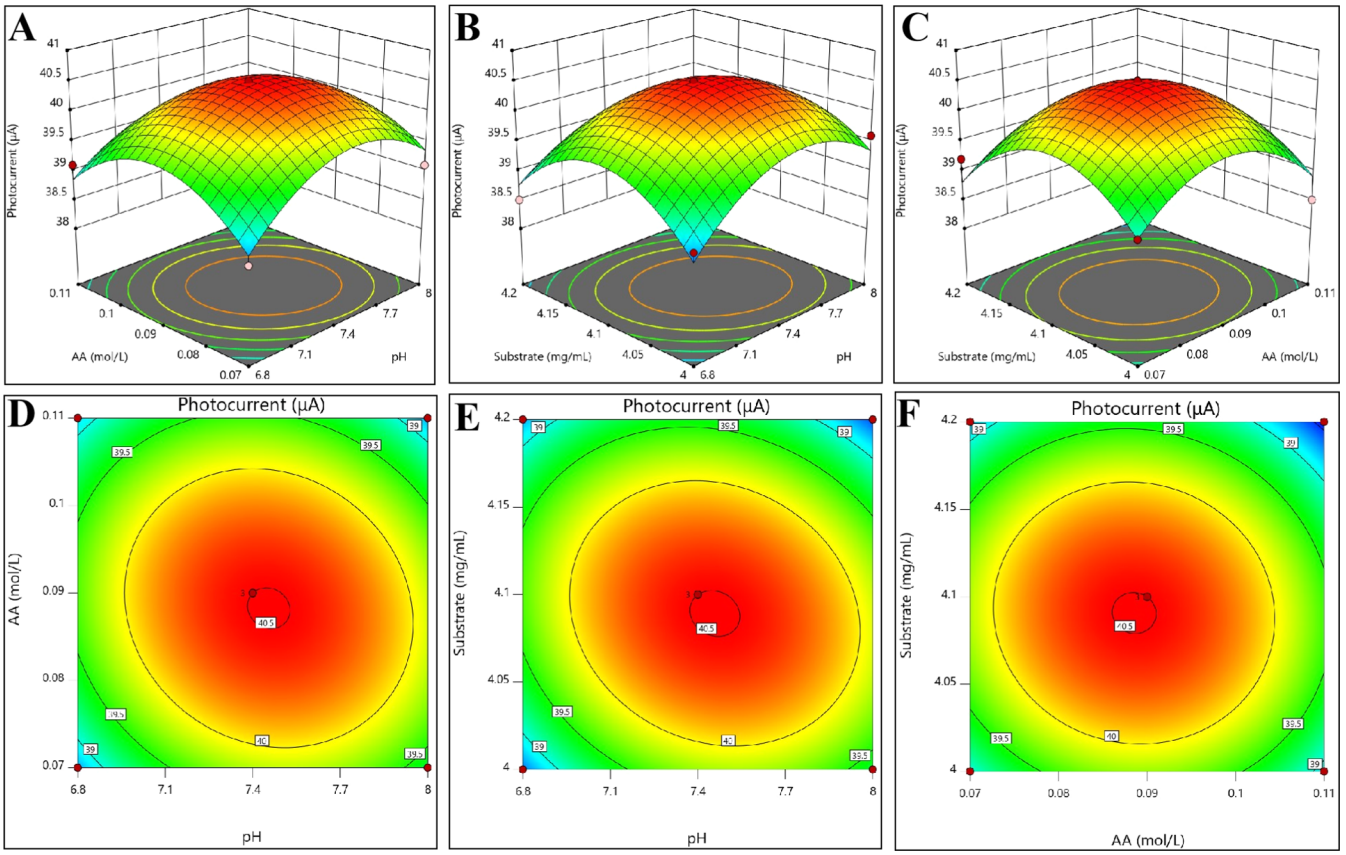

Figure 4. Box−Behnken experiments of AA concentration, pH, and substrate (Fe_2O_3/Cd-$ZnIn_{2.2}S_y$) concentration. (A−C) are the 3D images of two factors interacting with each other, and (D−F) are the contour maps of the interaction of the two factors.

(pH 7.4) containing 0.1 M ascorbic acid (electron donor). Figure 3A shows that the current response at Fe_2O_3 is 14.8 μA (curve a). However, the current response at Fe_2O_3/$ZnIn_{2.2}S_y$ is 24.5 μA (curve b) because the formation of the heterostructure between Fe_2O_3 and $ZnIn_{2.2}S_y$ enhances the photocurrent response. The current response at Fe_2O_3/Cd-$ZnIn_{2.2}S_y$ increases to 35.1 μA (curve c) because the Cd doping could improve the separation efficiency of the electron−hole pairs and further enhance the photocurrent response. The result indicates that Fe_2O_3/Cd-$ZnIn_{2.2}S_y$ shows good PEC performance. As shown in Figure 3B, the photocurrent intensity of NSE at a concentration of 100 fg/mL is 14.91 μA if the Ag@PANI-conjugated antibody is introduced. Otherwise, the photocurrent is only 9.84 μA. Therefore, the introduction of the Ag@PANI-conjugated antibody increases the photocurrent by 51.5%.

EIS Characterization of the Prepared Immunosensor. Electrochemical impedance spectroscopy (EIS) is an important method to investigate the successful construction of the PEC immunosensor. In the AC impedance test in this experiment, the concentration of NSE was 10 ng/mL. The experimental parameters are set as follows: the open-circuit potential (zero bias) is 0.18 V, the peak-to-peak amplitude of the AC potential is 5 mV, and the frequency range is 0.1−10,000 Hz. The Nyquist diagram of the AC impedance method is mainly composed of two parts: a linear part of the low-frequency region that corresponds to the limit of electrochemical diffusion and a feature in the high-frequency region that corresponds to the limit of electron transfer in the electrochemical process, and the diameter of the semicircle is related to the electron-transfer resistance. The inset of Figure 3C shows an equivalent circuit representing features of the electrode−electrolyte solution interface, which includes the charge-transfer resistance (R_{et}) of NSE, electrolyte resistance (R_s), double-layer capacitance (C_{dl}), and Warburg diffusion resistance (Z_w) that stands for diffusion resistance. In addition, ZSimpWin software was used to fit the EIS data, and the specific values were obtained as shown in Table S2. As shown in the Nyquist diagram of EIS (Figure 3C), the bare ITO exhibits a very small R_{et} (27.7 Ω) value (curve a). After continuous modification of Fe_2O_3/Cd-$ZnIn_{2.2}S_y$ (curve b) and Fe_2O_3/Cd-$ZnIn_{2.2}S_y$/PDA (curve c) on the bare ITO surface, the R_{et} values increased to 43.7 and 62.4 Ω, respectively, confirming their successful binding to the superior electrode. When antibody Ab_1 (curve d) is modified on the surface-functionalized electrode, the R_{et} value increases to 151 Ω due to the obstructive and insulating properties of the protein. After continuous modification of BSA (curve e), NSE (curve f), and Ag@PANI-Ab_2 (curve g), the R_{et} value gradually increased to 302 Ω (curve g). Therefore, these results prove that the PEC immunosensor has been prepared successfully.

Comparison of the Effective Active Area of Electrodes. Increasing the effective active area of the electrode is an effective way to enhance more reaction sites and improve the photocurrent response of the electrode. To compare the effective active area of Fe_2O_3/Cd-$ZnIn_{2.2}S_y$-coated ITO relative to that of ITO, we performed cyclic voltammetry at these electrodes with 5 mmol/L $[Fe(CN)_6]^{3-/4-}$ as the supporting electrolyte. The peak current of the voltammograms was then measured and plotted against the square root of the potential

https://doi.org/10.1021/acs.analchem.2c02645
Anal. Chem. 2022, 94, 17396−17404

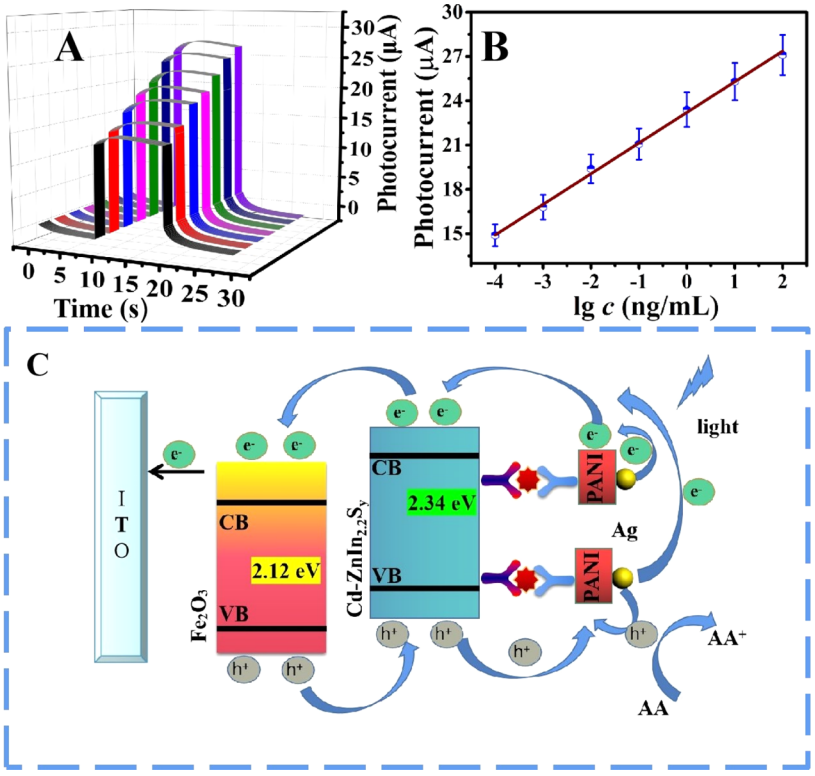

Figure 5. (A) Photocurrent corresponding to the operating curve points. (B) Logarithmic calibration plot of the immunosensor for different concentrations of NSE with the equation. (C) Electron-transfer mechanism of the sandwich-type PEC immunosensor.

scan rate. The results obtained are shown in Figure S5. According to the equation $I = (2.69 \times 10^5)AD^{1/2}n^{3/2}vc$, where I denotes the oxidation peak current value, A the electrochemically active electrode area (cm^2), D the diffusion coefficient "$[(6.70 \pm 0.02) \times 10^{-6}$ cm^2 $s^{-1}]$" of 5 mmol/L $[Fe(CN)_6]^{4-/3-}$ supporting electrolyte,[28] n is 1, v the scan rate, and c the concentration of $[Fe(CN)_6]^{4-/3-}$ solution, A can be evaluated from the slope of an I versus $v^{1/2}$ plot. In this way, from Figure S5A, it can be seen that the electrochemically active electrode surface area of the Fe_2O_3/Cd-$ZnIn_{2.2}S_y$-coated ITO was estimated to be 0.47 cm^2 while that of ITO was 0.35 cm^2, suggesting an increase of ~34%.

Optimization of Experimental Conditions. In order to obtain the best performance of the immunosensor, Figure 4 shows the optimization results obtained based on the following three main experimental conditions: the concentration of Fe_2O_3/Cd-$ZnIn_{2.2}S_y$, the concentration of AA, and the pH. The results are shown in Figure 4. Box−Behnken experiments were designed and optimized for substrate concentration, AA concentration, and pH. Specific experimental procedures are reported in the Supporting Information. As shown in Table S3, the pH ranges from 6.8 to 8.0, the AA concentration ranges from 0.07 to 0.11 M, and the Fe_2O_3/Cd-$ZnIn_{2.2}S_y$ concentration ranges from 4.0 to 4.2 mg/mL. The test data is simulated using Design Expert software. Table S4 shows the experimental data that needs to be tested. Figure 4A−C shows the simulated 3D image. The simulation equation is shown as follows: $I = 40.50 + 0.1250A - 0.1250B - 0.1750C - 0.1750AB - 0.2250AC - 0.0750BC - 0.7625A^2 - 0.8125B^2 - 0.9125C^2$. The best data is shown in Table S5. When the pH is 7.412, the AA concentration is 0.089 M, the substrate concentration is 4.098 mg/mL, and the photocurrent reached a maximum of 40.521 μA. Contours can be used to explain the interaction of several factors. When the contour tends to the ellipse, the interaction of the two factors is significant, and when the contour tends to the circle, the interaction of the two factors is not significant. As can be seen in Figure 4D−F, the three contours do not tend to be elliptic, which means no clear interaction between the three factors.

Performance of the PEC Immunosensor. A sandwich-type immunosensor for the detection of NSE is proposed by combining the advantages of the increased active area of the heterojunction structure with Fe_2O_3/Cd-$ZnIn_{2.2}S_y$ as a sensing platform and Ag@PANI as a signal amplification label. Under optimal experimental conditions, PEC experiments were conducted at the Fe_2O_3/Cd-$ZnIn_{2.2}S_y$-coated ITO with Ag@PANI as a signal amplification label. Figure 5A shows a plot of photocurrent obtained against time as the NSE concentration was increased from 100 fg/mL to 100 ng/mL. By plotting the steady-state photocurrent in Figure 5A against the logarithm of the NSE concentration, a linear calibration plot, shown in Figure 5B, was then obtained. The regression equation can be expressed as photocurrent = (2.07 ± 0.104) lg $c + 23.2 \pm 1.16$ ($R^2 = 0.996$; $N = 7$). Based on a signal-to-noise ratio of 3, the detection limit was estimated to be 33.5 fg/mL. As shown in Table S6, this method has a relatively wide detection range and a low detection limit compared to other methods for detecting NSE. Figure 5C illustrates the possible electron-transfer mechanism at ITO/Fe_2O_3/Cd-$ZnIn_{2.2}S_y$/Ag@PANI in PEC analysis. In order to determine the bandgap widths of Fe_2O_3 and Cd-$ZnIn_{2.2}S_y$, we carried out the solid UV diffuse reflection test, and the test results are shown in Figure S6A,B. The bandgap widths of Fe_2O_3 and Cd-$ZnIn_{2.2}S_y$ are 2.12 and 2.34 eV, respectively. The positions of the conduction and valence bands of Fe_2O_3 correspond to 0.30 and 2.42 eV,[14] respectively. The conduction and valence bands of Cd-$ZnIn_{2.2}S_y$ are −1.16

https://doi.org/10.1021/acs.analchem.2c02645
Anal. Chem. 2022, 94, 17396−17404

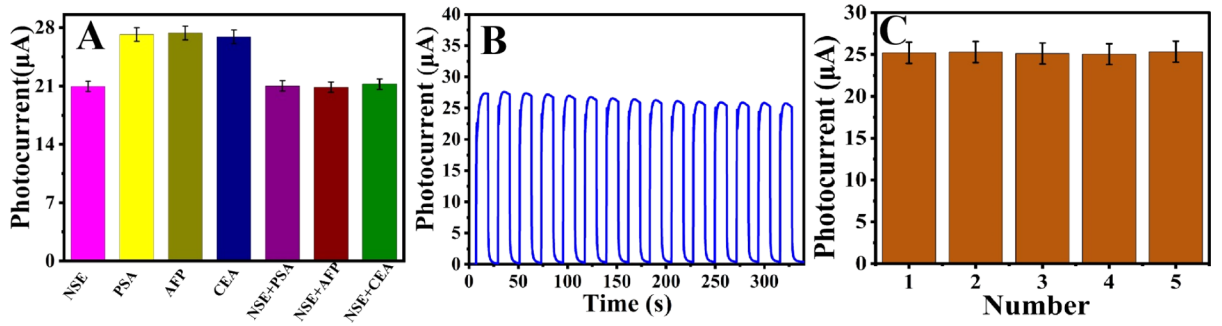

Figure 6. (A) Immunosensor specificity for NSE coexisting with interfering substances of PSA, AFP, and CEA. (B) Stability of the immunosensor over a continuous period of 350 s. (C) Reproducibility of the PEC immunosensor.

and 1.18 eV,[27] respectively. In addition, as shown in Figure S6C,D, Fe_2O_3 and Cd-$ZnIn_{2.2}S_y$ can absorb light below 663 and 546 nm, respectively. When light is shone on the working electrode, the e^-—h^+ pairs of Ag@PANI and Fe_2O_3/Cd-$ZnIn_{2.2}S_y$ are separated. The electrons generated by light leap from the HOMO orbital of PANI to the LUMO orbital, leaving holes in the HOMO orbital of PANI. The LUMO orbital of PANI has a more negative conduction band than Cd-$ZnIn_{2.2}S_y$, and Fe_2O_3 has the smallest conduction band position. This stepped energy level allows the electrons to quickly transfer to the Cd-$ZnIn_{2.2}S_y$ conduction band position and then to the Fe_2O_3 conduction band position in turn. Meanwhile, the holes in the valence band of Fe_2O_3 are transferred to the Cd-$ZnIn_{2.2}S_y$ valence band and the HOMO orbital of PANI in turn. Finally, the positively charged holes electrostatically interacted with the negatively charged ascorbate in the solution. Thus, the ascorbate promotes the effective separation of e^-—h^+ pairs, increases the photoelectric conversion efficiency, and improves the photocurrent response.

The specificity of the sandwich-type immunosensor was investigated by other cancer markers that may coexist with NSE [including prostate specific antigen (PSA), alpha fetoprotein (AFP), and carcinoembryonic antigen (CEA)] substances, and the results obtained are displayed in Figure 6A. Even though the other tumor markers were 100 times the concentration of NSE, the photocurrent response was a blank electrode. In addition, when there are other interfering substances mixed with NSE, the photocurrent response was similar to that measured in a blank solution. In addition, in the presence of an interfering substance—NSE mixture, a photocurrent of similar magnitude to that in NSE alone was obtained. We attribute this to the specific recognition of NSE by its antibody. This indicates that the proposed immunosensor has an ideal specificity for identifying NSE.

The stability of the immunosensor is one of the most important evaluation criteria.[29] To test the stability of the immunosensor, the constructed immunosensor was measured continuously for 350 s under optimal experimental conditions, and the light was turned on/off 17 times continuously (Figure 6B). After continuous irradiation, the photocurrent value of the immunosensor was observed to have changed by 6.47%.

In addition, the photocurrent response of the prepared sensor remained above 95% of the initial photocurrent value after 4 weeks of storage (Figure S7), so the constructed PEC immunosensor demonstrated the anticipated stability.

Reproducibility is an important indicator for testing PEC immunosensors. Therefore, we prepared five PEC immunosensors under the same conditions. The test conditions were carried out under optimal conditions, and the concentration of NSE was 10 ng/mL. The test results are shown in Figure 6C, and the measured currents of the five electrodes were 25.20, 25.30, 25.12, 25.06, and 25.35 μA, and the relative standard deviation is 0.48%. It shows that the PEC immunosensor has good reproducibility.

Sample Analysis. To evaluate the accuracy and feasibility of the sandwich-type immunosensor for real-life sample analysis, the recovery of two male serum samples for the NSE assay was performed by the standard addition method. As shown in Table 1, the recovery rate ranges from 95.2 to 106.0%, the and RSD ranges from 1.02 to 3.26% after analyzing the serum samples mixed with different concentrations of standard samples, respectively. It indicates that the immunosensor is reliable and accurate in real sample testing.

Table 1. Human Serum Sample Analysis of NSE

sample	added (ng/mL)	found (ng/mL)	recovery (n = 5, %)	RSD (n = 5, %)
1	0	6.72		
	1.00	7.67	95.2	2.55
	5.00	11.74	100.4	1.02
	10.00	16.78	100.6	1.24
2	0	7.15		
	1.00	8.23	108.0	3.26
	5.00	12.05	98.0	2.56
	10.00	17.34	101.9	2.37

CONCLUSIONS

In summary, a sandwich-type PEC immunosensor was constructed for the detection of NSE. The Fe_2O_3/Cd-$ZnIn_{2.2}S_y$ composite has a wide visible light absorption range to obtain more light energy, with a large-enough effective active area to provide more reaction sites and a large number of electron transport channels for fast electron transfer. Further, the introduction of Ag@PANI with strong electrical conductivity as an antibody marker realizes the signal amplification. The sensor also possesses excellent specificity and stability and high selectivity. The sensor exhibits a good linear detection range of 100 fg/mL to 100 ng/mL with a low detection limit of 33.5 fg/mL. Given these advantages, the immunosensor can be applied for the analysis of general tumor markers and will have a wide range of applications in the field of analytical chemistry.

https://doi.org/10.1021/acs.analchem.2c02645
Anal. Chem. 2022, 94, 17396−17404

■ ASSOCIATED CONTENT

Supporting Information

The Supporting Information is available free of charge at https://pubs.acs.org/doi/10.1021/acs.analchem.2c02645.

Materials and apparatus, SEM image of the materials, elemental mapping image of the Fe_2O_3/Cd-$ZnIn_{2.2}S_y$ electrode, energy-dispersive X-ray spectroscopy of Fe_2O_3/Cd-$ZnIn_{2.2}S_y$, XPS survey spectrum of O, linear relation between the peak reduction current I and the $v^{1/2}$ of ITO and Fe_2O_3/Cd-$ZnIn_{2.2}S_y$, bandgap and ultraviolet absorption curve of Fe_2O_3 and Fe_2O_3/Cd-$ZnIn_{2.2}S_y$, specific steps of the Box−Behnken experiment, storage stability of the immunosensor, and comparison of different methods for the detection of NSE (PDF)

■ AUTHOR INFORMATION

Corresponding Author

Xiang Ren − *Key Laboratory of Chemical Sensing & Analysis in Universities of Shandong, School of Chemistry and Chemical Engineering, University of Jinan, Jinan 250022, P. R. China; Collaborative Innovation Center for Green Chemical Manufacturing and Accurate Detection, Jinan 250022, P. R. China; State Key Laboratory of Analytical Chemistry for Life Science, College of Chemistry and Chemical Engineering, Nanjing University, Nanjing 210023, China;* orcid.org/0000-0002-4321-4282; Email: chem_renx@163.com

Authors

Jingui Chen − *Key Laboratory of Chemical Sensing & Analysis in Universities of Shandong, School of Chemistry and Chemical Engineering, University of Jinan, Jinan 250022, P. R. China*

Jinxiu Zhao − *Key Laboratory of Chemical Sensing & Analysis in Universities of Shandong, School of Chemistry and Chemical Engineering, University of Jinan, Jinan 250022, P. R. China*

Jinhui Feng − *Key Laboratory of Chemical Sensing & Analysis in Universities of Shandong, School of Chemistry and Chemical Engineering, University of Jinan, Jinan 250022, P. R. China*

Dan Wu − *Key Laboratory of Chemical Sensing & Analysis in Universities of Shandong, School of Chemistry and Chemical Engineering, University of Jinan, Jinan 250022, P. R. China; Collaborative Innovation Center for Green Chemical Manufacturing and Accurate Detection, Jinan 250022, P. R. China;* orcid.org/0000-0002-8732-5988

Hongmin Ma − *Key Laboratory of Chemical Sensing & Analysis in Universities of Shandong, School of Chemistry and Chemical Engineering, University of Jinan, Jinan 250022, P. R. China; Collaborative Innovation Center for Green Chemical Manufacturing and Accurate Detection, Jinan 250022, P. R. China;* orcid.org/0000-0002-7061-8944

Qin Wei − *Key Laboratory of Chemical Sensing & Analysis in Universities of Shandong, School of Chemistry and Chemical Engineering, University of Jinan, Jinan 250022, P. R. China; Collaborative Innovation Center for Green Chemical Manufacturing and Accurate Detection, Jinan 250022, P. R. China;* orcid.org/0000-0002-3034-8046

Huangxian Ju − *Collaborative Innovation Center for Green Chemical Manufacturing and Accurate Detection, Jinan 250022, P. R. China; State Key Laboratory of Analytical Chemistry for Life Science, College of Chemistry and Chemical Engineering, Nanjing University, Nanjing 210023, China;* orcid.org/0000-0002-6741-5302

Complete contact information is available at: https://pubs.acs.org/10.1021/acs.analchem.2c02645

Notes

The authors declare no competing financial interest.

■ ACKNOWLEDGMENTS

This study was supported by the National Natural Science Foundation of China (no. 22204059), the Natural Science Foundation of Shandong Province (nos. ZR2021QB120 and ZR2020QB097), the Foundation of Yunnan Key Laboratory of Rural Energy Engineering (Yunnan Normal University), and the Special Foundation for Taishan Scholar Professorship of Shandong Province (H.J. and Q.W.).

■ REFERENCES

(1) Neal, R. D.; Sun, F.; Emery, J. D.; Callister, M. E. *Br. Med. J.* **2019**, *365*, l1725.

(2) Iwama, E.; Okamoto, I.; Yabuuchi, H.; Takayama, K.; Harada, T.; Matsuo, Y.; Tokunaga, S.; Baba, E.; Nakanishi, Y. *J. Thorac. Oncol.* **2016**, *11*, 1586−1590.

(3) Dal Bello, M. G.; Filiberti, R. A.; Alama, A.; Orengo, A. M.; Mussap, M.; Coco, S.; Vanni, I.; Boccardo, S.; Rijavec, E.; Genova, C.; Biello, F.; Barletta, G.; Rossi, G.; Tagliamento, M.; Maggioni, C.; Grossi, F. *J. Transl. Med.* **2019**, *17*, 74.

(4) Wang, Y.; Zhao, P.; Mao, L.; Hou, Y.; Li, D. *RSC Adv.* **2018**, *8*, 3143−3150.

(5) Gao, X.; Zheng, P.; Kasani, S.; Wu, S.; Yang, F.; Lewis, S.; Nayeem, S.; Engler-Chiurazzi, E. B.; Wigginton, J. G.; Simpkins, J. W.; Wu, Wu. *Anal. Chem.* **2017**, *89*, 10104−10110.

(6) Zheng, Y.; Zhao, Y.; Di, Y.; He, L.; Liao, S.; Li, D.; Liu, X. *RSC Adv.* **2019**, *9*, 15513−15520.

(7) Sun, L.; Shen, K.; Zhang, J.; Wan, W.; Cao, W.; Wang, Z.; Guo, C. *RSC Adv.* **2021**, *11*, 32135−32142.

(8) Zang, Y.; Fan, J.; Ju, Y.; Xue, H.; Pang, H. *Chem* **2018**, *24*, 14010−14027.

(9) Zhao, C.-Q.; Ding, S.-N. *Coord. Chem. Rev.* **2019**, *391*, 1−14.

(10) Li, F.; Zhang, M.; Benetti, D.; Shi, L.; Besteiro, L. V.; Zhang, H.; Liu, J.; Selopal, G. S.; Sun, S.; Wang, Z.; Wei, Q.; Rosei, F. *Appl. Catal., B* **2021**, *280*, 119402.

(11) Zhang, M.; Li, F.; Benetti, D.; Nechache, R.; Wei, Q.; Qi, X.; Rosei, F. *Nano Energy* **2021**, *81*, 105626.

(12) Li, F.; Benetti, D.; Zhang, M.; Feng, J.; Wei, Q.; Rosei, F. *Small Methods* **2021**, *5*, 2100109.

(13) Li, L.; She, X.; Yi, J.; Pan, L.; Xia, K.; Wei, W.; Zhu, X.; Chen, Z.; Xu, H.; Li, H. *Appl. Surf. Sci.* **2019**, *469*, 933−940.

(14) Geng, Y.; Chen, D.; Li, N.; Xu, Q.; Li, H.; He, J.; Lu, J. *Appl. Catal., B* **2021**, *280*, 119409.

(15) Xu, W.; Xue, W.; Huang, H.; Wang, J.; Zhong, C.; Mei, D. *Appl. Catal., B* **2021**, *291*, 120129.

(16) Kafi, F. S. B.; Wijesundera, R. P.; Siripala, W. *Phys. Status Solidi A* **2020**, *217*, 2000330.

(17) Shim, S. G.; Tan, J.; Lee, H.; Park, J.; Yun, J.; Park, Y. S.; Kim, K.; Lee, J.; Moon, J. *Chem. Eng. J.* **2022**, *430*, 133061.

(18) Wu, P.; Liu, Z.; Chen, D.; Zhou, M.; Wei, J. *Appl. Surf. Sci.* **2018**, *440*, 1101−1106.

(19) Tian, C. M.; Li, W. W.; Lin, Y. M.; Yang, Z. Z.; Wang, L.; Du, Y. G.; Xiao, H. Y.; Qiao, L.; Zhang, J. Y.; Chen, L.; Qi, D.-C.; MacManus-Driscoll, J. L.; Zhang, J. L.; Zhang, K. L. *J. Phys. Chem. C* **2020**, *124*, 12548−12558.

(20) Liu, C.; Meng, F.; Zhang, L.; Zhang, D.; Wei, S.; Qi, K.; Fan, J.; Zhang, H.; Cui, X. *Appl. Surf. Sci.* **2019**, *469*, 276−282.
(21) Sharma, M. D.; Mahala, C.; Basu, M. *ACS Appl. Nano Mater.* **2021**, *4*, 3013−3021.
(22) Tan, C.; Sun, D.; Xu, D.; Tian, X.; Huang, Y. *Ceram. Int.* **2016**, *42*, 10997−11002.
(23) Chen, F. Z.; Zhu, Y. C.; Han, D. M.; Chen, H. Y. *ACS Appl. Bio Mater.* **2020**, *3*, 1761−1768.
(24) Abouelsayed, A.; Anis, B.; Eisa, W. H. *J. Phys. Chem. C* **2020**, *124*, 18243−18256.
(25) Huang, T.; Chen, W.; Liu, T.-Y.; Hao, Q.-L.; Liu, X.-H. *Powder Technol.* **2017**, *315*, 157−162.
(26) Chada, V. G.; Hausner, D. B.; Strongin, D. R.; Rouff, A. A.; Reeder, R. J. *J. Colloid Interface Sci.* **2005**, *288*, 350−360.
(27) Jia, H.; Cheng, S.; Zhang, H.; Yu, J.; Lai, Y. *Appl. Surf. Sci.* **2015**, *353*, 414−418.
(28) Feng, J.; Dai, L.; Ren, X.; Ma, H.; Wang, X.; Fan, D.; Wei, Q.; Wu, R. *Anal. Chem.* **2021**, *93*, 7125−7132.
(29) Zhang, J.; Xue, X.; Du, Y.; Zhao, J.; Ma, H.; Ren, X.; Wei, Q.; Ju, H. *Anal. Chem.* **2022**, *94*, 12368−12373.

https://doi.org/10.1021/acs.analchem.2c02645
Anal. Chem. 2022, 94, 17396−17404